Deformation of *sd*-shell nuclei derived from inelastic scattering of 50 MeV α particles

J. Fritze, R. Neu, H. Abele, F. Hoyler, and G. Staudt
Physikalisches Institut der Universität Tübingen, D 7400 Tübingen, Federal Republic of Germany

P. D. Eversheim and F. Hinterberger
Institut für Strahlen- und Kernphysik der Universität Bonn, D 5300 Bonn, Federal Republic of Germany

H. Müther
Institut für Theoretische Physik der Universität Tübingen, D 7400 Tübingen, Federal Republic of Germany
(Received 17 September 1990)

Differential cross sections for elastic and inelastic α scattering on ^{19}F, ^{20,22}Ne, and ^{23}Na have been measured at 50 MeV. The data have been analyzed in the coupled-channel approach considering the model of a symmetric rotor together with the double-folding model for the optical potential. As an alternative also a Woods-Saxon parametrization for the radial shape of the real part of the optical potential has been considered. Both parametrizations yield similar results for the quadrupole and hexadecapole moments. These isoscalar multipole moments are consistent with those obtained from electromagnetic probes and with the predictions of microscopic shell-model calculations. Large deformations are needed to describe the enhancement of the elastic-scattering cross section at backward angles for ^{20,22}Ne.

I. INTRODUCTION

In a systematic study of elastic and inelastic α scattering on light nuclei at energies near 50 MeV we first investigated the elastic scattering on ^{11}B, ^{12,13}C, ^{14,15}N, ^{16,17,18}O, ^{20}Ne, and ^{24}Mg in the framework of the optical model.[1] Double-folded α nucleus potentials calculated by means of a density-dependent form of the M3Y effective nucleon-nucleon interaction[2] have been used to analyze the data. It could be shown that the experimental data are rather well described in a wide range of energies for target nuclei in the mass region $13 \leq A \leq 18$.

The case of the elastic α-^{20}Ne scattering turned out to be different. It was impossible to reproduce the rise of the cross section observed in the experiment at backward angles using a potential consistent with the α-^{16}O fit. Exchange effects between the incident α particle and the weakly bound α cluster in ^{20}Ne may cause the observed anomaly. These effects can be simulated by a parity-dependent potential as recently shown by Michel and Reidemeister[3] in the analysis of our α-^{20}Ne data at 54.1 MeV. Allowing for a very small parity splitting in the real part of the potential, it is possible to obtain a precise description of the observed enhancement at back angles. An optical model analysis of α-^{20}Ne elastic cross sections at four energies, including also experimental data at 27.3, 33.0, and 80.7 MeV (Refs. 4 and 5) utilizing a parity-dependent double-folding potential, has shown that this parity splitting decreases with increasing energy.[6]

On the other hand, it is well known that *sd*-shell nuclei in the region around $A = 20$ are strongly deformed. The low-lying natural-parity states can be explained reasonably well in terms of the collective, rotational model. These states are strongly populated by Coulomb excitation as well as by electron and hadron scattering. Experimental data on elastic and inelastic scattering of protons,[7–11] deuterons (Refs. 12 and 13), ^{3}He (Refs. 14 and 15), and α particles[16–20] on ^{19}F, ^{20,22}Ne, and ^{23}Na have successfully been interpreted by coupled-channel (CC) calculations in which the optical potential is assumed to be nonspherical, according to the shape of the matter distributions. Evidence is found for ground-state quadrupole and hexadecapole deformation using the so-called Satchler theorem[21–23] which connects multipole moments of the matter distribution to those of the optical potential.[10,24–26]

In a study of elastic and inelastic α scattering on ^{24}Mg it was found recently[27] that an optical-model (OM) analysis cannot be expected to describe the angular distribution for elastic scattering over the entire angular range. For larger angles, discrepancies are observed between the OM fits and the experimental data. On the other hand, CC calculations based on double-folded α-^{24}Mg potentials give a good overall agreement with the experimental data. Therefore, strong coupling effects between the elastic channel and the inelastic ones may also be responsible for the observed backward rise in the elastic α-^{20}Ne cross section.

In the present investigation we measured the elastic and inelastic α scattering on ^{19}F, ^{20}Ne, and ^{22}Ne at an incident energy of 54 MeV and on ^{23}Na at 48 MeV. First, the elastic data are analyzed in the framework of the conventional optical model. Double-folded α potentials are used in these calculations. Second, the results of the present experiment are analyzed within the CC method using the quadrupole and hexadecapole transition amplitudes evaluated from the symmetric-rotational model. Both, deformed Woods-Saxon and double-folded α poten-

 ©1991 The American Physical Society

tials are used in the CC analysis.

Using the Satchler theorem isoscalar charge moments are extracted from the deformation parameters of the CC analyses. The corresponding isoscalar transition rates and quadrupole moments are compared with shell-model predictions and published $B(E\lambda)$ values deduced from electromagnetic probes.

II. EXPERIMENT

The cross-section data were taken at the isochronous cyclotron facility of the University of Bonn. The α-particle beam was focused at the center of a 50-cm-diameter scattering chamber. Beam intensities between 10 nA and 1 μA were used with an energy resolution of 5×10^{-4}. For the target nuclei ^{19}F, ^{20}Ne, and ^{22}Ne the beam energy was 54.1 MeV, whereas for ^{23}Na it was 48.7 MeV.

LiF and NaCl targets of about 50 and 100 μg/cm^2 thickness, respectively, were used for this experiment. The targets were produced by evaporation onto thin carbon foils. For the other target nuclei, isotopically enriched ^{20}Ne and ^{22}Ne gases were used contained in a cylindrical gas cell of 60 mm diameter. The gas pressure was about 500 mbar and was monitored continuously.

The detector system consisted of four E detectors mounted on two turntables rotating around the target. The detectors were of the surface-barrier type with a thickness of about 2000 μm. The dead time was monitored continuously with a random pulser. The spectra were accumulated in a computer and stored on magnetic tapes for further off-line processing. The overall energy resolution was about 250 keV FWHM for the ^{20}Ne and ^{22}Ne runs and about 200 keV FWHM for the ^{19}F and ^{23}Na experiments. A peak-fitting technique was applied to separate the ground state and the excited state at 0.2 MeV in ^{19}F (see Fig. 1). The evaluation of the measurements with the gas target followed closely the procedure outlined by Silverstein.[28]

Data were accumulated at laboratory angles from about 9° to 35° in 0.5° steps, from about 35° to 70° in 1° steps, and from about 70° to 160° in 2° steps. The zero-degree direction could be fixed with an accuracy of 0.12° by methods described in Ref. 1.

Beam monitoring was accomplished in the usual way by means of a Faraday cup and by a monitor additionally built in the scattering chamber. For the exact normalization of the absolute cross sections, the elastic-scattering data in forward direction were adjusted to optical-model predictions. This procedure is justified since elastic scattering in forward direction is dominated by the Coulomb interaction. Therefore, the optical-model parameters can be varied in a wide reasonable range without changing the resulting normalization.

III. OPTICAL-MODEL ANALYSIS

The absolute differential cross sections of the elastic-scattering processes obtained in the present study are shown in Fig. 2 together with elastic-scattering data on ^{16}O and ^{20}Ne which have already been measured in our earlier experiment.[1] Whereas for ^{16}O (in accordance with

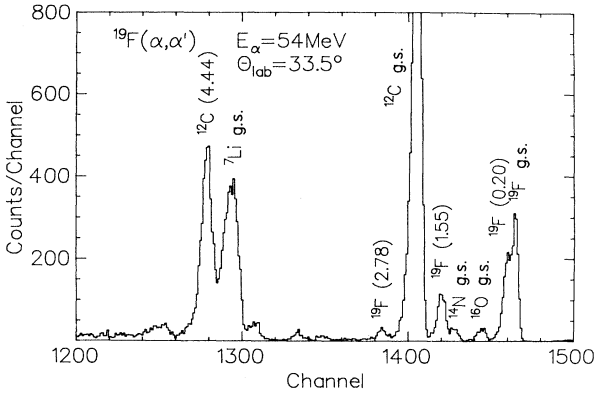

FIG. 1. Typical LiF-α spectrum at 33.5°.

the results[1] on ^{14,15}N and ^{17,18}O) a decrease of the cross section at backward angles is observed, the ^{20}Ne(α,α) angular distribution is characterized by a strong backward rise beyond $\Theta_{c.m.}\simeq110°$. Now we find that similar to this well-known behavior of the α-^{20}Ne process, an enhancement at larger angles can also be observed in the elastic scattering on ^{22}Ne and less pronounced for ^{19}F and ^{23}Na, as well.

For the OM analysis of the elastic-scattering data, the complex potential used has the standard form

$$U(r)=-V(r)-iW(r)+V_c(r)\ . \tag{1}$$

The real part of the nuclear potential is described by a

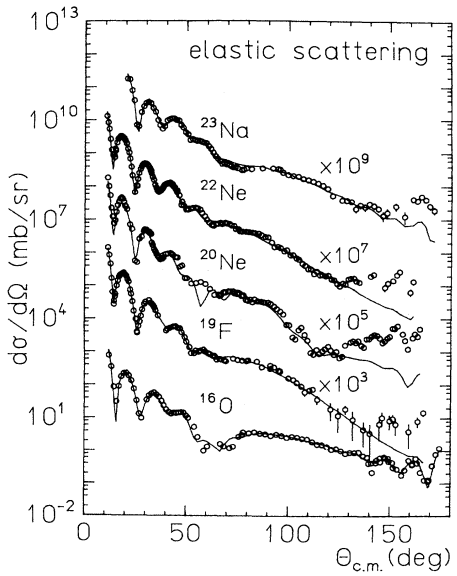

FIG. 2. Elastic α scattering on ^{16}O (Ref. 1), ^{19}F, ^{20}Ne, and ^{22}Ne at 54.1 MeV and on ^{23}Na at 48.7 MeV: Experimental data and optical-model fits, calculated by using the double-folding potential.

double-folding ansatz

$$V(r) := U_F(r) = \lambda_f \int d\mathbf{r}_1 \int d\mathbf{r}_2 \rho_T(\mathbf{r}_1)\rho_\alpha(\mathbf{r}_2) \times t(E,\rho_T,\rho_\alpha,\mathbf{s}=\mathbf{r}+\mathbf{r}_2-\mathbf{r}_1) , \quad (2)$$

where $\mathbf{r}$ is the separation of the centers of mass of the colliding target nucleus and the α particle, $\rho_T(\mathbf{r}_1)$ and $\rho_\alpha(\mathbf{r}_2)$ are the respective nucleon densities, and λ_f is an overall normalization factor. For the effective interaction t, the density-dependent form of the M3Y nucleon-nucleon interaction[2] has been chosen. In this work we assume the neutron distribution to be N/Z times the proton one. Therefore we used for the density distribution of the target nuclei ρ_T the experimental charge distribution obtained from electron scattering[29] after having it unfolded from the finite charge distribution of the proton. For the density of the α particle a Gaussian form was used.[30] Details of the computation of the potential $U_F(r)$ are described in Ref. 1.

The imaginary part of the potential was chosen in a "model-independent" form as a Fourier-Bessel series of six terms[1]

$$W(r) = \sum_{k=1}^{6} a_k j_0(k\pi r/R_c) \quad (3)$$

with a cutoff radius $R_c = 10$ fm.

All fits were performed using the computer-code GOMFIL,[31] where the only adjustable parameters are the six Fourier-Bessel coefficients a_k of the imaginary part and the normalization constant λ_f of the real part of the potential.

The results of the calculations are shown as smooth curves in Fig. 2. The differential cross sections for the elastic α scattering on ^{16}O are in excellent agreement with experiment. This result is well known and it is valid in a broad energy range from 30 up to 150 MeV.[1] On the other hand, the OM analysis obviously fails to reproduce the experimental data for larger angles for the target nuclei ^{19}F, ^{20,22}Ne, and ^{23}Na, thus indicating that more complicated reaction mechanisms are involved.

The normalization factor λ_f, the volume integrals, and the rms radii of the optical potentials obtained by the fitting procedure are listed in Table I together with the ^{16}O data adopted from Table 3 of Ref. 1. The values for λ_f and consequently the volume integrals for the real part of the potential $J_R/4A$ are found to be somewhat lower for the nuclei ^{19}F, ^{20,22}Ne and ^{23}Na than those obtained for the nitrogen and oxygen isotopes,[1] but they correspond to the ^{24}Mg results.[27] On the other hand, the large values of the volume integrals $J_I/4A$ of the imaginary part of the potential, obtained for ^{19}F, ^{20,22}Ne, and ^{23}Na reflect a strong absorptivity of these nuclei due to their high collectivity.

IV. COUPLED-CHANNEL ANALYSIS

A. CC calculations within the symmetric-rotor model

The nuclei ^{19}F, ^{20,22}Ne, and ^{23}Na are the lightest nuclei in the *sd* shell which are considered to be permanently deformed. Thus, the excitation of low-lying positive-parity states can be treated within the collective rotational model. For the elastic and inelastic scattering on deformed nuclei, coupled-channel calculations are adequate to analyze the experimental data. In the CC calculations the alpha-nucleus interaction is described by a deformed optical potential $V(r,R(\Omega))$. Assuming an axial-symmetric quadrupole and hexadecapole deformation, the radius parameter $R(\Omega')$ in the body-fixed system is angle-dependent according to

$$R(\Omega') = R_0[1+\beta_2 Y_{20}(\Omega')+\beta_4 Y_{40}(\Omega')] . \quad (4)$$

The coupling potentials V_{cp}, defined by

$$V(r,R(\Omega)) = V_{\text{diag.}}(r) + V_{cp}(r,\Omega) \quad (5)$$

are derived from the Legendre expansion of the deformed interaction potential $V(r,R(\Omega'))$ transformed from the body-fixed (Ω') to the space-fixed (Ω) system

$$V_{cp}(r,\Omega) = \sum_{\substack{\lambda,\mu \\ \lambda\neq 0}} v_{\lambda 0}(r) D^{\lambda}_{\mu 0}(\varepsilon_i) Y_{\lambda\mu}(\Omega) , \quad (6)$$

where $D^{\lambda}_{\mu 0}(\varepsilon_i)$ are the Wigner rotation matrices and ε_i the Euler angles. Following Tamura[32] the coupling matrix elements can be evaluated as

$$\langle l_f I_f | V_{cp} | l_i I_i \rangle = \sum_{\lambda\neq 0} v_{\lambda 0}(r) \langle I_f \| D^{\lambda}_{;0} \| I_i \rangle A(l_f I_f, l_i I_i, \lambda I) , \quad (7)$$

where $A(l_f I_f, l_i I_i, \lambda I)$ is an angular momentum factor

TABLE I. Normalization factor λ_f of the double-folding α-nucleus potential for the real interaction as well as volume integrals and rms radii for the optical-model analysis of the elastic scattering on ^{16}O, ^{19}F, ^{20}Ne, ^{22}Ne, and ^{23}Na.

Target nucleus	E_{lab} (MeV)	λ_f	$J_R/4A$ (MeV fm^3)	$\langle r_R^2\rangle^{1/2}$ (fm)	$J_I/4A$ (MeV fm^3)	$\langle r_I^2\rangle^{1/2}$ (fm)
^{16}O	54.1	1.35	383.5	3.61	76.6	4.28
^{19}F	54.1	1.19	334.8	3.75	118.2	4.55
^{20}Ne	54.1	1.20	350.2	3.87	130.1	4.43
^{22}Ne	54.1	1.15	325.9	3.88	119.8	4.37
^{23}Na	48.7	1.15	330.4	3.91	106.0	4.50

explicitly given by Tamura[32] and $v_{\lambda 0}(r)$ is the radial form factor

$$v_{\lambda 0}(r)=\int V(r,R(\Omega'))Y_{\lambda 0}(\Omega')d\Omega' \tag{8}$$

describing the radial shape of the transition potential (6) for the excitation of collective states. The reduced matrix elements $\langle I_f \| D^{\lambda}_{;0} \| I_i \rangle$ can be calculated in consideration of the Wigner-Eckhard theorem. Using the wave functions of a symmetric rotor we get

$$\langle I_f \| D^{\lambda}_{;0} \| I_i \rangle = (2I_i+1)^{1/2}(I_i \lambda K 0 | I_f K) , \tag{9}$$

where K is the projection of the total angular momentum on the symmetry axis of the core. The numerical values are $K=1/2$ for ^{19}F, $K=0$ for ^{20}Ne and ^{22}Ne, and $K=3/2$ for ^{23}Na.

In the coupled-channel calculations both Woods-Saxon and double-folded alpha-nucleus potentials have been used. The size and shape of the deformed Woods-Saxon potential is parameterized in the usual way by introducing expansion (4) for the radius parameter $R_0=r_0 A^{1/3}$ for both the real and imaginary parts of the potential. In order to gain a properly deformed folding potential, in the first step the potential calculated by the double-folding procedure is expanded in a Fourier-Bessel series of 10 terms. Now both the real and imaginary parts of the potential are described by Fourier-Bessel functions as given by Eq. (3). Subsequently, in the second step the cutoff radius R_c is expressed by expansion (4). In all calculations the Coulomb potential is deformed in the usual way. In the CC calculations which were performed using a modified version of the computer code ECIS,[33] all states displayed in Figs. 3–6 have been included. Due to the

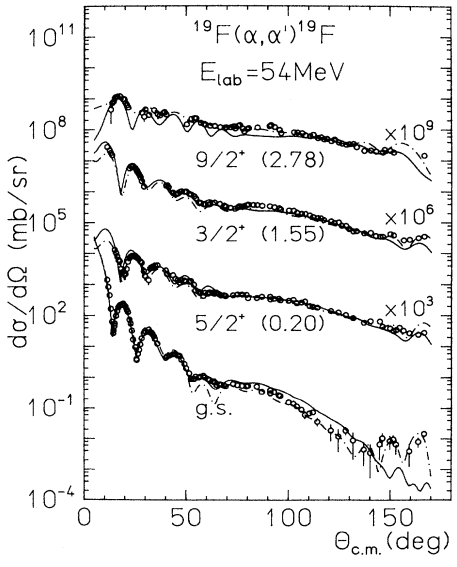

FIG. 3. Elastic and inelastic α scattering on ^{19}F at 54.1 MeV: Experimental data and CC analysis fits calculated with the double-folded potential (solid lines) and a Woods-Saxon potential (dash-dotted lines). All states have been included in the calculations.

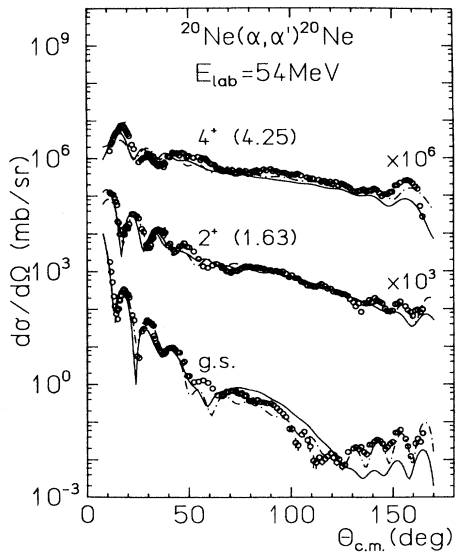

FIG. 4. Same as Fig. 3, but for α scattering on ^{20}Ne at 54.1 MeV.

Coriolis term[34] in the collective Hamiltonian, an inversion of the level sequence is observed for the higher members of the $K=1/2^+$ rotational band of the nucleus ^{19}F. In order to complete the coupling equations for the $L=4$ and $L=2$ transitions in ^{19}F and ^{23}Na, respectively, in the CC analysis for both nuclei the coupling to the $7/2^+$ state has been taken into account additionally.

In the fit procedure the deformation parameters β_2 and β_4 as well as the optical potential parameters were adjusted in order to obtain an optimum reproduction of the experimental cross-section data. In the CC analysis of the ^{23}Na data only a quadrupole deformation was taken into account. In all fits the deformation of the real and imagi-

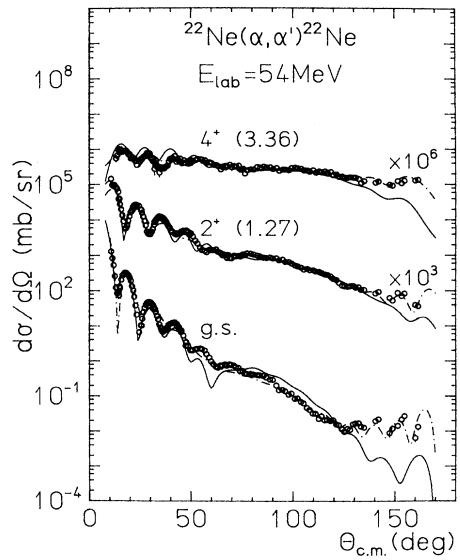

FIG. 5. Same as Fig. 3, but for α scattering on ^{22}Ne at 54.1 MeV.

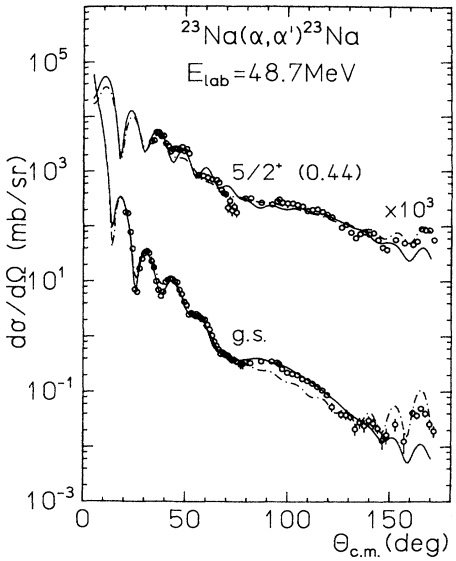

FIG. 6. Same as Fig. 3, but for α scattering on ^{23}Na at 48.7 MeV.

nary potential as well as the Coulomb potential was assumed to be the same.

The final results are shown in Figs. 3–6 together with the experimental data. The best-fit values of the optical potential parameters are listed in Table II, those of the deformation parameters β_2 and β_4 are given in Table III, together with the resulting volume integrals and rms radii of the potentials. Since the shape of the deformed Woods-Saxon potential is different from that of the deformed folding potential, different values for the deformation parameters result in the analysis for the same nucleus. We shall find, however, in the following section that the multipole moments of both, the deformed Woods-Saxon and the folding potential are similar.

B. Isoscalar transition rates and quadrupole moments

For an axial-symmetric mass distribution $\rho(\mathbf{r})$ the normalized multipole moments can be written in the body-fixed system as

$$q_{\lambda 0} := \int \rho(\mathbf{r}) r^{\lambda} Y_{\lambda 0}(\Omega') d\mathbf{r} \quad \text{with} \quad \int \rho(\mathbf{r}) d\mathbf{r} = 1 \ . \tag{10}$$

According to the so-called Satchler theorem,[21–23] the normalized mass distribution can be replaced by a normalized potential, if the real part V_R of the effective scattering potential can be described by a folding ansatz with a density-independent effective *NN* interaction (implicit folding procedure). In this case we get

$$q_{\lambda 0} = \frac{1}{J_R} \int v_{\lambda 0}(r) r^{\lambda+2} dr \tag{11}$$

with the volume integral J_R and with $v_{\lambda 0}(r)$ given in Eq. (8).

In reality the effective *NN* interaction is density dependent and Eq. (11) has to be corrected accordingly. Within the method of implicit folding these corrections have been calculated[35,36] to be in the order of a few percent for quadrupole excitations. Recent explicit folding calculations[37,38] for inelastic α scattering, accounting also for dynamic density dependence, give even smaller corrections. Therefore, we used Eq. (11) without any corrections for the density dependence.

Assuming that neutron and proton deformations are the same, we get the charge moments $m_{\lambda 0}$ for a symmetric rotor by multiplying the normalized potential moments $q_{\lambda 0}$ with the charge Ze

$$m_{\lambda 0} := Z e q_{\lambda 0} = \frac{Ze}{J_R} \int v_{\lambda 0}(r) r^{\lambda+2} dr \ . \tag{12}$$

The deduced $q_{\lambda 0}$ and $m_{\lambda 0}$ themselves are isoscalar moments $q_{IS\lambda 0}$ and $m_{IS\lambda 0}$, respectively, since the alpha particle is an isoscalar probe. Now the reduced $IS\lambda$ matrix elements for a transition $I_i \rightarrow I_f$ can be evaluated after transforming the $IS\lambda$ moments into the space-fixed system

$$M_{IS\lambda}(I_i \rightarrow I_f) = i^{\lambda} m_{IS\lambda 0} \langle I_f \| D^{\lambda}_{;0} \| I_i \rangle \tag{13}$$

using the reduced matrix elements $\langle I_f \| D^{\lambda}_{;0} \| I_i \rangle$ defined in Eq. (9).

The $IS\lambda$ transition probability is then given by the $B(IS\lambda)$ value as

$$B(IS\lambda, I_i \rightarrow I_f) = (2I_i+1)^{-1} M^2_{IS\lambda}(I_i \rightarrow I_f) \ . \tag{14}$$

TABLE II. Best-fit parameters of the α-nucleus optical potentials for the coupled-channel analysis of the elastic and inelastic scattering on ^{19}F, ^{20}Ne, ^{22}Ne, and ^{23}Na. Top: Parameters of the Woods-Saxon potentials. Bottom: Normalization factor λ_f of the double-folding potential for the real interaction and Fourier-Bessel coefficients for the imaginary part of the potential.

	V (MeV)	r_R (fm)	a_R (fm)	W (MeV)	r_I (fm)	a_I (fm)	
^{19}F	124.9	1.24	0.77	9.2	2.02	0.43	
^{20}Ne	93.6	1.51	0.70	10.9	1.92	0.44	
^{22}Ne	136.1	1.10	0.79	21.4	1.29	0.76	
^{23}Na	121.6	1.26	0.77	14.8	1.61	0.65	
	λ_f	a_1	a_2	a_3	a_4	a_5	a_6
^{19}F	1.298	7.77	10.69	3.68	3.35	9.86	6.84
^{20}Ne	1.309	6.59	6.51	−0.86	−5.34	−4.48	−1.66
^{22}Ne	1.257	7.58	7.62	−2.34	0.19	9.86	5.54
^{23}Na	1.251	8.34	10.46	−1.06	−3.92	3.06	1.11

TABLE III. Deformation parameters, volume integrals and rms radii for both the double-folding and Woods-Saxon optical potentials used in the CC analysis of the elastic and inelastic α scattering on ^{19}F, ^{20}Ne, ^{22}Ne at 54.1 MeV and on ^{23}Na at 48.7 MeV.

Target nucleus	Potential	β_2	β_4	$J_R/4A$ (MeV fm^3)	$\langle r_R^2\rangle^{1/2}$ (fm)	$J_I/4A$ (MeV fm^3)	$\langle r_I^2\rangle^{1/2}$ (fm)
^{19}F	Double folding	0.234(2)	0.041(4)	365.8	3.75	92.1	4.58
	Woods-Saxon	0.312(6)	0.078(8)	384.3	3.84	84.4	4.47
^{20}Ne	Double folding	0.265(3)	0.059(5)	381.6	3.86	86.4	5.16
	Woods-Saxon	0.320(3)	0.066(4)	435.8	4.10	83.2	4.52
^{22}Ne	Double folding	0.254(3)	0.022(3)	357.9	3.88	81.6	4.86
	Woods-Saxon	0.430(7)	0.046(3)	312.5	3.77	68.8	3.96
^{23}Na	Double folding	0.230(4)		359.0	3.91	82.3	4.62
	Woods-Saxon	0.357(10)		371.2	3.97	76.6	4.28

Finally, the diagonal elements of the $IS\lambda$ matrix are related to the spectroscopic quadrupole moments of the excited nuclei

$$Q_I=\left[\frac{16\pi}{5}\frac{I(2I-1)}{(I+1)(2I+1)(2I+3)}\right]^{1/2}M_{IS2}(I\rightarrow I)\ . \tag{15}$$

[We note, that in our preceding paper (Ref. 27) this expression has been written incorrectly.] The factor Ze in Eq. (12) enables a direct comparison of our $B(IS\lambda)$ values with $B(E\lambda)$ values and electric quadrupole moments deduced from electromagnetic interactions. In Tables IV and V we compare the deduced $B(IS\lambda)$ values and the static quadrupole moments Q_I with experimental

TABLE IV. $B(IS2)$ and $B(E2)$ values in units of e^2 fm^4 as well as static quadrupole moments Q_2 in units of e fm^2 for ^{19}F, ^{20}Ne, ^{22}Ne, and ^{23}Na.

			$B(IS2)$ Rotational model		$B(E2)$ Shell model[a]			
			folding	Woods-Saxon			e.m. Expt.	
	I_i	I_f	potential	potential	0.4e	0.5e	b	c
^{19}F	5/2	1/2	35.9±1.6	29.0±2.5	20.8	26.8	20.9±0.2	
	3/2	1/2	35.9±2.0	29.0±3.0	20.7	26.7	20.8±1.5[d]	
	3/2	5/2	15.4±15	12.4±5.3	8.9	11.6		
	9/2	5/2	51.3±22	41.4±3.4	20.3	26.5	24.7±2.7	
	7/2	3/2	46.2	37.3	21.5	27.3		
	7/2	5/2	5.1	4.1	2.1	2.7		
	7/2	9/2	3.9	3.1	2.4	3.3		
^{20}Ne	2	0	67.9±2.6	69.0±2.3	55.0	68.0	65.5±3.2	68±6
	4	2	97.1±4.8	98.6±4.1	65.4	80.7	71.0±6.5	
^{22}Ne	2	0	57.8±2.2	52.1±2.6	52.8	66.3	47.6±3.7[d]	46±2
	4	2	82.5±3.9	74.5±4.1	71.5	88.9	65.9±3.7[d]	
^{23}Na	5/2	3/2	95.5±5.3	111±34	114	141	77.7±10[d]	105±8[e]
	7/2	3/2	39.8	46.3	41.4	51.5	48±8[e]	
	7/2	5/2	59.7	69.5	63.8	79.2	51±12[e]	
			Quadrupole moments Q_2					
^{19}F	5/2		−12.1±2.1	−10.9±1.6	−10.0	−11.3	−12±2	
	3/2		−8.5±2.0	−7.6±1.6	−6.4	−7.3		
^{20}Ne	2		−16.7±1.9	−16.8±1.0	−15.1	−16.8	−23±3[f]	
	4		−21.2±5.0	−21.4±2.3	−19.1	−21.2		
^{22}Ne	2		−15.4±1.9	−14.6±0.7	−14.5	−16.2	−19±4[f]	
	4		−19.6±5.3	−18.6±1.5	−18.3	−20.5		
^{23}Na	3/2		10.6±0.8	11.4±8.0	11.1	12.4	10.1±0.2[g]	
	5/2		−3.8±3.8	−4.1±3.7	−2.7	−3.1		

[a]This work, effective isoscalar charge of 0.4e and 0.5e, respectively.
[b]Reference 39.
[c]Reference 40.
[d]Reference 41.
[e]Reference 42.
[f]Reference 43.
[g]Reference 44.

TABLE V. $B(IS4)$ and $B(E4)$ values in units of e^2 fm^8 for ^{19}F, ^{20}Ne, ^{22}Ne, and ^{23}Na.

			$B(IS4)$ Rotational model		$B(E4)$ Shell model[a]		
	I_i	I_f	folding potential	Woods-Saxon potential	0.4e	0.5e	e.m. Expt. b
^{19}F	9/2	1/2	2770±180	2180±171	836	1088	937±210
	7/2	1/2	2770±180	2180±171	954	1209	
^{20}Ne	4	0	9060±1000	6080±900	3310	4090	4260±930
^{22}Ne	4	0	2960±300	806±200	1501	1716	1890±455 [c]
^{23}Na	5/2	3/2	235±85	377±128	297	341	
	7/2	3/2	1056±380	1697±611	281	314	

[a]This work, effective isoscalar charge of 0.4e and 0.5e, respectively.
[b]Reference 41.
[c]Reference 48.

$B(E\lambda)$ values[39–42] and electric quadrupole moments Q_2 (Refs. 39, 43, and 44) as well as with the results of our shell-model calculations. The uncertainties on the $B(IS\lambda)$ values from this work result from the errors on the β_l parameters entering Eq. (10) as given by the code ECIS[33] and the effect of a χ^2-fit procedure using a fixed deformation of the potential, where the individual transition matrix elements of all transitions leading to a specific state have been varied simultaneously.

For the shell-model calculations we assume an inert core of ^{16}O and consider all possible configurations of three (^{19}F), four (^{20}Ne), six (^{22}Ne), and seven (^{23}Na) valence nucleons in the states of the $1s0d$ shell,[45] respectively. The single-particle energies for the valence states with respect to the ^{16}O core were deduced from the empirical energies of nuclei with a mass number $A=17(\varepsilon_i=-4.15,\ -3.28$, and 0.93 MeV for $i=0d_{5/2}$, $1s_{1/2}$, and $0d_{3/2}$, respectively). For the residual interaction between valence nucleons we have chosen the A-dependent effective interaction proposed by Wildenthal.[46] The transition rates and quadrupole moments have been evaluated assuming single-particle oscillator functions with an oscillator length of $b=1.82$ fm and an additional effective isoscalar charge of 0.4e and 0.5e, respectively.

V. DISCUSSION

The comparison of the experimental data with the results of the coupled-channel calculations shows better agreement for calculations using Woods-Saxon potentials (dash-dotted lines in Figs. 3–6) than for those using double-folding potentials (solid lines in Figs. 3–6). This is especially true for the elastic-scattering data.

The calculations using a Woods-Saxon potential reproduce the experimental data for all transitions over the full angular range fairly well. This means obviously, that in contrast to the double-folding potentials the parametrization of Woods-Saxon potentials is flexible enough to allow for an individual adjustment to the experimental data for each nucleus. On the other hand, no systematic behavior can be deduced from the parameters (Table II) and the resulting volume integrals and rms radii (Table III) obtained from these individual best-fit calculations.

The real part of the double-folding potential is determined entirely by the folding procedure except the normalization factor λ_f. From our optical-model analysis of experimental data on the nuclei ^{13}C, ^{14,15}N, and ^{16,17,18}O it is known, that the resulting volume integrals of these potentials are almost mass independent and have a value of approximately 375 MeV fm^3 for this energy.[1] A very similar value was found in the CC analysis of the elastic and inelastic α scattering on ^{24}Mg at the same beam energy.[27]

In Fig. 7 the volume integrals of the real (double folding) and the imaginary (Fourier-Bessel) parts of the α nucleus potential for the nuclei studied in this investigation are presented along with the results on the nuclei mentioned above. The results of the OM analysis (Fig. 2, Table I) are shown as open circles and the CC calcula-

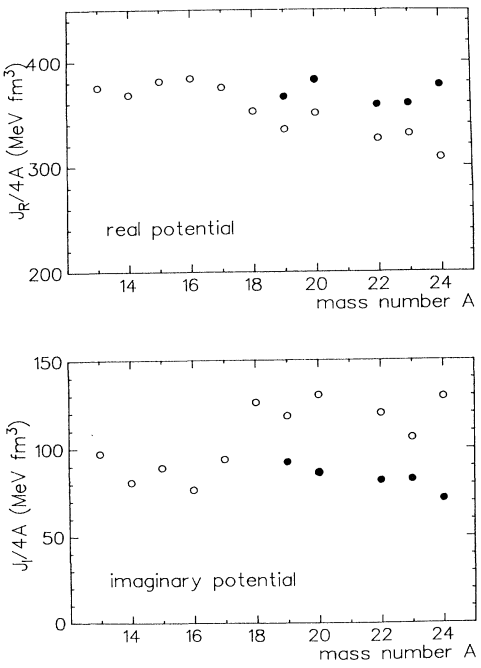

FIG. 7. Volume integrals for the real and imaginary part of the double-folding α-nucleus potential for OM calculations (open circles) and CC analysis (solid circles).

tions (Figs. 3–6, Table III) as solid circles. The volume integrals obtained from the imaginary potentials in the CC calculations are systematically smaller than the corresponding values calculated for the OM analysis. This is consistent with the expectation that those contributions to the imaginary part of the OM which are due to the coupling to the channels taken into account explicitly in the CC analysis, should be absent in the imaginary part obtained in the CC calculation. The explicit treatment of certain channels in the CC calculations yields an enhancement of the real part at the energies under consideration. These observations are consistent with those of Ref. 27. It can be inferred from Fig. 7 that the values for J_R and J_I deduced from our CC calculation fit very well into the systematics obtained for the neighboring nuclei.

These systematic fits of angular distributions for elastic and inelastic α scattering in the CC analysis using the double-folded potentials do not reproduce the rise of the elastic cross sections at backward angles. The cross sections obtained in the calculation, where experimental data of all channels are considered in the fit, tend to fall off too steeply in the elastic channel for backward angles. In order to demonstrate that this discrepancy can be removed, we consider again the case of ^{20}Ne, for which the backward rise of the elastic channel is the largest. The solid line in Fig. 8(a) represents the results of a CC calculation using the double-folding potential for which the fit has been restricted to reproduce the elastic channel. This fit reproduces the experiment very nicely including the data at backward angles. The fit, however, requires a normalization constant $\lambda_f = 1.386$ ($J_R/4A = 404$ MeV fm^3, $J_I/4A = 80.3$ MeV fm^3) which is considerably larger than those obtained for the neighboring nuclei. Furthermore, the deformation obtained in this fit ($\beta_2 = 0.346$, $\beta_4 = 0.048$) is so large that the cross section for the excited states is strongly overestimated [see Fig. 8(a)].

Our CC calculations show so far, that it is not possible to get a correct description for the cross sections of the excited states and the backward rise of the elastic scattering simultaneously, by enlarging the deformation and varying the imaginary part of the potential. The result, which represents an optimal compromise is also shown in Fig. 8(a) (dashed line). In this calculation λ_f was chosen to be 1.365 ($J_R/4A = 398$ MeV fm^3) and $\beta_2 = 0.293$, $\beta_4 = 0.049$ ($J_I/4A = 80.25$ MeV fm^3). With this deformed potential the excited states are described still fairly well and the angular distribution of the elastic scattering shows a pronounced backward rise, underestimating however the experimental data by a factor of about 4. For comparison Fig. 8(a) also shows the result obtained from a fit to all data (Fig. 4) as a dashed dotted line. In Fig. 8(b) the radial behavior of the corresponding imaginary part of the potentials is shown.

All this demonstrates that it is possible to reproduce the backward rise of the elastic scattering cross section in a calculation which contains enough free parameters. This could be an OM calculation using a potential depending on parity, a CC calculation employing a Woods-Saxon potential or a CC calculation in the double-folding

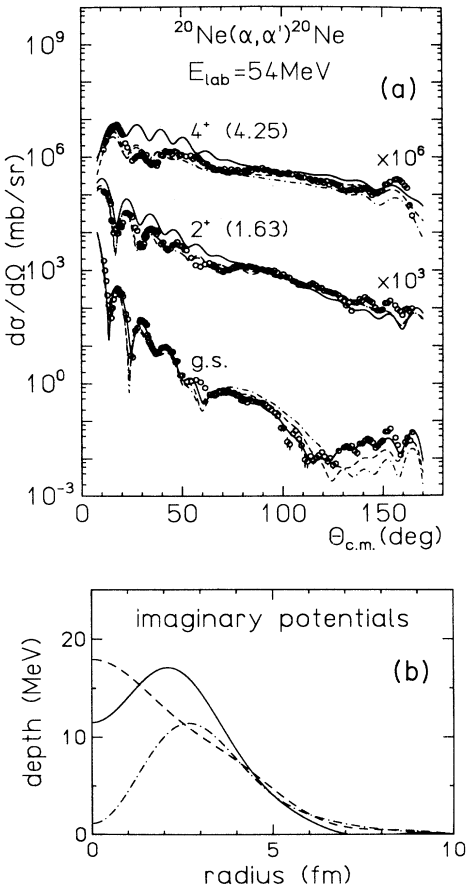

FIG. 8. (a) Comparison of different CC calculations using the same coupling scheme. Solid line: only data for the g.s. transition are used in fit, dash-dotted line: best fit using all experimental data (see Fig. 4), dashed line: optimal compromise. (b) Radial dependence of the imaginary part of the corresponding potentials used for the fits shown in (a).

model (with fewer parameters) enforcing the fit to the elastic channel. For a deeper understanding of the physical mechanism which is responsible for this backward rise, it seems necessary to perform calculations which include the analysis of inelastic scattering to excited states and contain only a few parameters which either vary smoothly with nucleon number (λ_f) or can be related to other observables (β_2,β_4). Since such calculations do not yet lead to a satisfactory description of the backward rise, one may conclude that more complicated reaction mechanisms (e.g., α-cluster exchange) have to be considered to achieve a correct description of the empirical phenomena.

These arguments lead us to conclude that the following statements on nuclear collective deformation deduced from the parameters of our folding potentials have a systematic uncertainty of about 10–20%, as long as the physical reason for the observed backward rise of the angular distributions in elastic scattering is not understood. In Fig. 9(a) we present the isoscalar moments q_{20} calcu-

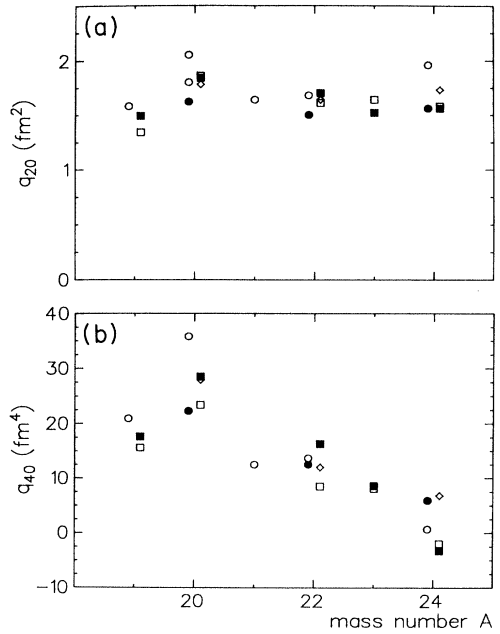

FIG. 9. Normalized quadrupole (a) and hexadecapole (b) moments, q_{20} and q_{40} ■ this work and Ref. 27, folding potential; □ this work and Ref. 27, Woods-Saxon potential; ◇(α,α') 104 MeV Refs. 25 and 17; ●(p,p') 800 MeV Refs. 10 and 26; ○$(p,p')\approx 30$ MeV Refs. 8, 9, and 47.

lated according to Eq. (12) using the deformed potential from Tables II and III, together with q_{20} obtained from published (p,p') and (α,α') data. Even though the deformation parameter β_2 varies from 0.23 between the folded potential of ^{23}Na and 0.43 for the Woods-Saxon (WS) potential for ^{22}Ne, the quadrupole moments are almost constant for the nuclei investigated, with the exception of the moment of ^{19}F, independent of the potentials and the projectile. This confirms the statement given already in Ref. 27, that the basic spectroscopic information is contained in the multipole moments and not in the deformation parameters β_2 and β_4, which depend strongly on the ansatz for the potential.

In Table IV the isoscalar transition probabilities $[B(IS\lambda)]$ and the static quadrupole moments as derived from Eqs. (14) and (15) are compared with the experimental values from electromagnetic probes and the results of our shell-model calculation. The shell-model calculation using an effective isoscalar charge of $0.4e$ agrees very well with the experimental data for the $B(E2)$ values for all investigated nuclei and underestimates only slightly the static quadrupole moments. (We note that the second $7/2^+$ state obtained in shell-model calculations for ^{19}F has been used to compare with the rotational model.) The CC calculations in the symmetric-rotor model also agree very well with the experimental $B(E2,2_1^+\rightarrow 0_1^+)$ values for the nuclei ^{20}Ne to ^{23}Na, but overestimate the $B(E2,4_1^+\rightarrow 2_1^+)$ in ^{20}Ne and ^{22}Ne by about 30%. For ^{19}F both parametrizations (folding and WS) yield $B(IS2)$ values, which are too high in comparison with the results from electromagnetic probes. This is to be expected since ^{19}F has two valence neutrons outside an ^{16}O core, contributing directly to $B(IS2)$, but only one valence proton, contributing to $B(IS2)$ and $B(E2)$.

As for the quadrupole moments the hexadecapole moments obtained from different hadronic probes result in very similar values. This is evidenced in Fig. 9(b). In Table V we present also the results for the isoscalar hexadecapole transition probabilities in comparison with the experimental results from (e,e') and the shell model. Again the shell model is in very good agreement with the values from the electromagnetic probe. The $B(IS4)$ values deduced from our inelastic α-scattering data are systematically too large compared to both, the shell model and the (e,e') results. On the other hand, the isoscalar transition probabilities follow the relative change in $\Delta L=4$ strength for the investigated nuclei rather closely. In this context it should be mentioned that one obtains also for ^{23}Na a nonvanishing hexadecapole moment, even though the deformation parameter β_4 was kept zero, because the $l=2$ deformation gives rise to a $\lambda=4$ moment in second (and higher) order when expansion (4) is inserted in (8). A reanalysis of the data measured at 42 MeV for ^{23}Na (from Ref. 20) including the $7/2^+$ and $9/2^+$ states and a free deformation parameter β_4 gave very similar values for q_{20} and q_{40}.

VI. CONCLUSIONS

Differential cross sections for the elastic and inelastic scattering of α particles at an incident energy of about 50 MeV have been measured for the $1s0d$-shell nuclei ^{19}F, ^{20,22}Ne, and ^{23}Na. These data have been analyzed in the framework of the optical model and of the coupled-channel formalism in the symmetric-rotor model. Woods-Saxon as well as double-folded optical potentials have been used in this study. The greater flexibility in the Woods-Saxon parametrization results in better fits to the shape of the angular distributions, but the best-fit parameters vary in a nonsystematic way. The real part of the double-folded potentials has only one free parameter, the normalization factor λ_f, and one obtains a smooth variation for the integral quantities as the volume integrals and rms radii and for the deformation parameters. Both potential parametrizations result in comparable quadrupole and hexadecapole moments despite big differences in the deformation parameters β_l. These results show that the deformation parameters β_l strongly depend on the geometry chosen in the optical potentials. Since the radial dependence of the double-folded potential is obtained from experimentally determined charge distributions, the deformation of these potentials are more likely to correspond to the actual deformation of the matter distribution of these light nuclei.

The extracted isoscalar quadrupole transition strengths and spectroscopic moments are in good agreement with the results from electromagnetic probes except for ^{19}F. This can be understood from the fact that ^{19}F contains two valence neutrons but only one valence proton outside the ^{16}O core. Furthermore, the symmetric-rotor model represents certainly an oversimplification for the case of

^{19}F since it has only three particles in the *sd* shell and the model contains no particle core interaction.

Even though the hexadecapole moments are not very precisely determined in inelastic α scattering at this energy, very similar values are obtained from other hadronic probes, which seem to be systematically higher than those obtained from (e,e'). The results from this study are not accurate enough to decide whether this deviation is due to differences between the charge and the mass distributions or to other reasons.

Very large deformation parameters are needed in CC calculations in order to reproduce the enhancement of the angular distributions for ^{20,22}Ne at backward angles. From this results a systematic uncertainty of about 10 to 20 % in the deduced isoscalar multipole moments for these nuclei. Further experimental studies at higher incident energies and the investigation of possible explanations as, e.g., exchange effects, are needed to understand this behavior.

ACKNOWLEDGMENTS

The cooperation of the Bonn Isochronous Cyclotron team is gratefully acknowledged. This work has been funded by the German Federal Minister for Research and Technology at Bundesministerium für Forschung und Technologie (BMFT) under Contract No. 06 Tü243.

[1]H. Abele, H. J. Hauser, A. Körber, W. Leitner, R. Neu, H. Plappert, T. Rohwer, G. Staudt, M. Strasser, S. Welte, M. Walz, P. D. Eversheim, and F. Hinterberger. Z. Phys. A **326**, 373 (1987).

[2]A. M. Kobos, B. A. Brown, R. Lindsay, and G. R. Satchler, Nucl. Phys. **A425**, 205 (1984).

[3]F. Michel and G. Reidemeister, Z. Phys. A **333**, 331 (1989).

[4]A. A. Cowley, J. C. Van Staden, S. J. Mills, P. M. Cronje, G. Heymann, and G. F. Burdzik, Nucl. Phys. **A301**, 429 (1978).

[5]M. Reed, Ph.D. thesis, University of California, Report UCRL-18414, 1968.

[6]H. Abele, R. Neu, J. Fritze, and G. Staudt, Verhandlg. DPG(VI) **24**, KD 2.5 (1989); H. Abele, R. Neu, and G. Staudt, Proceedings of the International Nuclear Physics Conference, Sao Paulo, 1989 (unpublished).

[7]R. de Swiniarski, C. Glashausser, D. L. Hendrie, J. Sherman, A. D. Bacher, and E. A. McClatchie, Phys. Rev. Lett. **23**, 317 (1969).

[8]R. de Swiniarksi, A. Genoux-Lubain, G. Bagieu, J. F. Cavaignac, and D. H. Worledge, Phys. Lett. **43B**, 27 (1973).

[9]R. de Swiniarski, F. G. Resmini, D. L. Hendrie, and A. D. Bacher, Nucl. Phys. **A261**, 111 (1976).

[10]G. S. Blanpied, B. G. Ritchie, M. L. Barlett, R. W. Fergerson, G. W. Hoffmann, and J. A. McGill, Phys. Rev. C **38**, 2180 (1988).

[11]M. C. Munro, G. G. Shute, B. M. Spicer, G. N. Taylor, A. D. Bacher, G. P. A. Berg, C. C. Foster, R. Sawafta, E. J. Stephenson, W. E. Dollhopf, and J. Keren, Scient. and Techn. Report 1988/89, Indiana University Cyclotron Facility, p. 24 (1989) (unpublished).

[12]D. Dehnhard and N. M. Hintz, Phys. Rev. C **1**, 460 (1970).

[13]J. Nurzynski, T. Kihm, K. T. Knöpfle, G. Mairle, and H. Clement, Nucl. Phys. **A465**, 365 (1987).

[14]K. P. Artemov, V. Z. Goldberg, and V. P. Rudakov, Yad. Fiz. **9**, 266 (1969) [Sov. J. Nucl. Phys. **9**, 157 (1969)]; **9**, 1173 (1969) [**9**, 686 (1969)].

[15]R. de Swiniarski, G. Bagieu, A. J. Cole, P. Gaillard, A. Guichard, J. Y. Grossiord, M. Gusakow, and J. R. Pizzi, J. Phys. (Paris) **35**, L25 (1974).

[16]G. Hauser, R. Löhken, H. Rebel, G. Schatz, G. W. Schweimer, and J. Specht, Nucl. Phys. **A128**, 81 (1969).

[17]H. Rebel, G. W. Schweimer, G. Schatz, J. Specht, R. Löhken, G. Hauser, D. Habs, and H. Klewe-Nebenius, Nucl. Phys. **A182**, 145 (1972).

[18]H. Rebel and G. W. Schweimer, Z. Phys. **262**, 59 (1973).

[19]T. P. Krick, N. M. Hintz, and D. Dehnhard, Nucl. Phys. **A216**, 549 (1973).

[20]M. C. Mannion, B. R. Fulton, S. D. Hoath, J. M. Nelson, C. A. Ogilvie, P. J. Woods, D. W. Banes, and K. I. Pearce, J. Phys. G **14**, 1093 (1988).

[21]G. R. Satchler, J. Math. Phys. **13**, 1118 (1972).

[22]R. S. Mackintosh, Nucl. Phys. **A266**, 379 (1976).

[23]H. Rebel, Z. Phys. A **277**, 35 (1976).

[24]S. Kato, K. Okada, M. Kondo, K. Hosono, T. Saito, N. Matsuoka, K. Hatanaka, T. Noro, S. Nagamachi, H. Shimizu, K. Ogino, Y. Kadota, S. Matsuki, and M. Wakai, Phys. Rev. C **31**, 1616 (1985).

[25]D.K. Srivastava and H. Rebel, KfK Report 3708, 1984 (unpublished).

[26]G. S. Blanpied, B. G. Ritchie, M. L. Barlett, G. W. Hoffmann, J. A. McGill, E. C. Milner, K. W. Jones, S. K. Nanda, and R. de Swiniarski, Phys. Rev. C **37**, 1987 (1988).

[27]R. Neu, S. Welte, H. Clement, H. J. Hauser, G. Staudt, and H. Müther, Phys. Rev. C **39**, 2145 (1989).

[28]E. Silverstein, Nucl. Instrum. Methods **4**, 53 (1959).

[29]H. de Vries, C. W. de Jager, and C. de Vries, At. Data Nucl. Data Tables **36**, 495 (1987).

[30]G. R. Satchler and W. G. Love, Phys. Rep. **55**, 183 (1979).

[31]H. Leeb, computer code GOMFIL (unpublished).

[32]T. Tamura, Rev. Mod. Phys. **37**, 679 (1965).

[33]J. Raynal, computer code ECIS (unpublished).

[34]L. Zetta and L. Zuffi, Nuovo Cimento **47A**, 141 (1978).

[35]D. K. Srivastava and H. Rebel, Z. Phys. A **316**, 225 (1984).

[36]H. Clement, G. Graw, H. Kader, F. Merz, H. J. Scheerer, P. Schiemenz, and N. Seichert, Nucl. Phys. **A451**, 219 (1986).

[37]D. K. Srivastava and H. Rebel, J. Phys. G **10**, L127 (1984).

[38]M. El-Azab Farid and G. R. Satchler, Nucl. Phys. **A481**, 542 (1988).

[39]F. Ajzenberg-Selove, Nucl. Phys. **A475**, 1 (1987).

[40]S. Raman, C. H. Malarkey, W. T. Milner, C. W. Nestor, Jr., and P. H. Stelson, At. Data Nucl. Data Tables **36**, 1 (1987).

[41]P. M. Endt, At. Data Nucl. Data Tables **23**, 3 (1979).

[42]D. Schwalm, E. K. Warburton, and J. W. Olness, Nucl. Phys. **A293**, 425 (1977).

[43]R. H. Spear, Phys. Rep. **73**, 369 (1981).

[44]B. Jeckelmann, W. Beer, I. Beltrami, F. W. N. de Boer, G. de

Chambrier, P. F. A. Goudsmit, J. Kern, H. J. Leisi, W. Ruckstuhl, and A. Vacchi, Nucl. Phys. **A408**, 495 (1983).
[45]R. R. Whitehead, A. Watt, B. J. Cole, and I. Morrison, Adv. Nucl. Phys. **9**, 123 (1977).
[46]B. H. Wildenthal, Prog. Part. Nucl. Phys. **11**, 5 (1983).
[47]D. K. Hasell, N. E. Davison, T. N. Nasr, B. T. Murdoch, A. M. Sourkes, and W. T. H. van Oers, Phys. Rev. C **27**, 482 (1983).
[48]X. K. Maruyama and F. J. Kline, Phys. Rev. C **19**, 1624 (1979).